

# Fully-coupled continuum damage model for simulation of plasticity dominated hydrogen embrittlement mechanisms

Robin Depraetere<sup>\*</sup>, Wim De Waele, Stijn Hertelé

Ghent University, Department of Electromechanical, Systems and Metal Engineering, Soete Laboratory, Technologiepark-Zwijnaarde 46, 9052 Zwijnaarde, Belgium

## ARTICLE INFO

### Keywords:

Hydrogen embrittlement  
Finite element analysis  
Coupled simulation  
Gurson model  
Diffusion

## ABSTRACT

The mechanical properties of steel are degraded due to the presence of hydrogen, also known as hydrogen embrittlement (HE). Simulations of hydrogen embrittlement at a continuum level can assist in characterizing the detrimental effect that is associated with the introduction of hydrogen regarding the structural integrity of steel structures. Such simulations require the implementation of both hydrogen diffusion and hydrogen assisted material degradation. The present study presents a framework for finite element simulations combining these aspects in a fully coupled way, with diffusion driven by hydrogen concentration, stress triaxiality gradient and plastic strain rate, and damage based on the ductile damage model known as the Complete Gurson Model (CGM). Hydrogen assisted degradation is modeled through acceleration of void growth, nucleation or coalescence, based on the HELP or HESIV mechanisms as underlying physical basis. The proposed model is the first fully-coupled continuum micromechanics-based damage model that accounts for the plasticity dominated HE mechanisms. The effect of element size and time increments is evaluated, establishing guidelines to use the model. Moreover, results of simulations of a tensile test on a hydrogen charged notched specimen are given, to provide an illustrative example of the capabilities of the framework. The well-known ductility loss due to hydrogen is observed in the simulation results.

## 1. Introduction

According to the European Green Deal, which strives for Europe to be the first climate-neutral continent by 2050, hydrogen has the potential to play a key role in the transition towards a low-carbon economy [1]. An important contribution hereto is the planned use of the current (mostly fossil fuel) pipeline network for the transportation and storage of renewable energy, in the form of hydrogen gas. However, a major attention point associated with the structural integrity of the infrastructure is the well-acknowledged hydrogen assisted mechanical degradation of metals, often referred to as hydrogen embrittlement (HE) [2]. In particular, the reduction in ductility and fracture toughness as a result of hydrogen deserves attention, and their impact on the safety of the structure has to be assessed. Although the phenomenon is known for a long time [3] and has been extensively investigated, consensus is lacking about the dominant damage mechanism which governs hydrogen embrittlement. Several theories have been proposed [4], including Hydrogen Enhanced DEcohesion (HEDE), Hydrogen Enhanced Localized Plasticity (HELP) and Hydrogen Enhanced Strain-Induced Vacancy (HESIV). HEDE argues that the cohesive strength of the steel lattice is weakened due to interstitial hydrogen [5], while HELP hypothesizes that atomic hydrogen enhances

the dislocation mobility, thereby facilitating plasticity at stress raisers such as crack tips [6]. HESIV on the other hand claims that hydrogen promotes the formation of vacancies upon straining, and thereby decreases the resistance against ductile crack growth [7].

Hydrogen embrittlement has been investigated numerically at diverse length scales, ranging from atomistic models [8–12] over mesoscopic models [12–14] to continuum models [11,12,15,16]. Whereas simulations at an atomic scale can assist in establishing fundamental knowledge about microstructural mechanisms [12], simulations at a continuum level can be of great benefit in predicting the structural response of hydrogenated steel structures. Despite increased interest and extensive research in recent years, modeling HE remains challenging [17].

The hydrogen embrittlement phenomenon is a complex coupled stress-diffusion mechanism, consisting of hydrogen redistribution throughout the steel lattice and an altered mechanical response as a result of hydrogen. These two processes influence each other. On the one hand, hydrogen diffusion is driven by not only the concentration gradient, but also by the hydrostatic stress gradient and plastic strain. On the other hand, the mechanical response depends on the local

<sup>\*</sup> Corresponding author.

E-mail address: [robidpra.Depraetere@UGent.be](mailto:robidpra.Depraetere@UGent.be) (R. Depraetere).

**Nomenclature****List of symbols**

$C_L$	Lattice hydrogen concentration [ $\text{m}^{-3}$ or wppm]
$C_T$	Trapped hydrogen concentration [ $\text{m}^{-3}$ or wppm]
$D_L$	Lattice diffusivity coefficient [ $\text{m}^2/\text{s}$ ]
$E$	Young's modulus [MPa]
$E_B$	Trap binding energy [J/mol]
$f$	Void volume fraction [–]
$\dot{f}$	Void volume growth [1/s]
$f_0$	Initial void volume fraction [–]
$f_c$	Critical void volume fraction [–]
$f_N$	Void volume fraction of nucleating particles [–]
$f^*$	Effective void volume fraction [–]
$[J]$	Jacobian matrix [m]
$\mathbf{J}_q$	Heat flux vector [J/(s m <sup>2</sup> )]
$k_{g,L}, k_{g,T}$	Hydrogen assisted degradation factors accelerating void growth [1/wppm]
$k_{n,L}, k_{n,T}$	Hydrogen assisted degradation factors accelerating void nucleation [1/wppm]
$K_T$	Constant for equilibrium between lattice and trapped hydrogen [–]
$l_c$	Element size at critical region [m]
$N^i$	Shape function
$N_A$	Avogadro constant [ $\text{mol}^{-1}$ ]
$N_L$	Lattice site density [ $\text{m}^{-3}$ ]
$N_T$	Trapping site density [ $\text{m}^{-3}$ ]
$n$	Strain hardening exponent [–]
$q$	External heat source [J/(s m <sup>3</sup> )]
$q_1, q_2, q_3$	Empirical constants CGM [–]
$r$	Void space ratio [–]
$R$	Gas constant [J/(mol K)]
$s_N$	Standard deviation of nucleating strain [–]
$t$	Time [s]
$T$	Temperature [K]
$U$	Internal energy [J/kg]
$\bar{V}_H$	Partial molar volume of hydrogen [ $\text{m}^3/\text{mol}$ ]
$V_M$	Molar volume of the host lattice [ $\text{m}^3/\text{mol}$ ]
$x, y, z$	Global coordinates [m]
$\alpha$	Number of hydrogen residing sites per trap [–]
$\alpha^T, \beta^T$	Fitted Thomason's constants [–]
$\beta$	Number of interstitial lattice sites per metal atom [–]
$\epsilon_N$	Mean nucleating strain [–]
$\epsilon_p$	Equivalent plastic strain [–]
$\zeta$	Minimum fraction of flow stress reduction due to hydrogen [–]
$\theta_L$	Lattice occupancy [–]
$\theta_T$	Trapped occupancy [–]
$\nu$	Poisson's ratio [–]
$\xi$	Hydrogen softening parameter [–]
$\xi', \eta', \zeta'$	Local coordinate system [–]

$\rho$	Density [ $\text{kg}/\text{m}^3$ ]
$\sigma$	Stress tensor [MPa]
$\sigma_e$	Von Mises stress [MPa]
$\sigma_h$	Hydrostatic stress [MPa]
$\sigma_0$	Yield strength [MPa]
$\sigma_1$	Maximum principal stress [MPa]
$\bar{\sigma}$	Flow stress [MPa]
$\bar{\sigma}_H$	Locally reduced flow stress due to hydrogen [MPa]

**List of acronyms**

CGM	Complete Gurson Model
CZM	Cohesive Zone Modeling
HE	Hydrogen Embrittlement
HEDE	Hydrogen Enhanced DEcohesion
HELP	Hydrogen Enhanced Localized Plasticity
HESIV	Hydrogen Enhanced Strain-Induced Vacancy

This ‘hydrogen induced dilatational strain’ is typically neglected for steel, since multiple authors have concluded that the solubility of hydrogen in ferrite is too low to cause a dilatational strain effect on the mechanical constitutive behavior [18,19].

The complex stress-diffusion interaction can be numerically described by either an uncoupled approach, or using a fully coupled approach. The uncoupled approach typically consists of three subsequent analysis steps [15,20–24], and therefore fails to capture the full interaction between hydrogen concentration and stress, since the analyses are performed sequentially. The fully coupled approach of hydrogen embrittlement simulations is an improvement of the uncoupled approach and requires customized codes [25–28]. The stress and diffusion equations are simultaneously solved, resulting in a coupling between the mechanical constitutive response and the hydrogen distribution.

An essential ingredient for hydrogen embrittlement simulations at a continuum level is the degrading effect of hydrogen on the material's mechanical properties. For simulating accelerated damage evolution, a damage mechanism affected by the hydrogen concentration must be implemented. Most research concerning continuum level hydrogen embrittlement simulations make use of Cohesive Zone Modeling (CZM) [15,16,20,21,24,27,29–31]. In such approach, specific cohesive elements are introduced at the anticipated crack path, accommodating a certain cohesive strength. The effect of hydrogen is introduced by decreasing this cohesive strength with increased hydrogen concentration. Most attempts of this implementation are based on the HEDE mechanism [30]. Certain drawbacks are associated with this approach. First of all, a predefined crack path is required. Secondly, CZM does not implicitly include the effect of stress triaxiality on damage development, but instead requires a user-defined triaxiality dependence of the cohesive strength [32]. More recently, Martínez-Pañeda et al. [33,34] applied the phase-field approach for simulating hydrogen embrittlement as an alternative to CZM. This approach starts from Griffith's thermodynamic balance and is therefore also linked with HEDE.

Despite the successful use of CZM and phase-field approaches for modeling HE, they are primarily based on the brittle HEDE mechanism. HE is also manifested through plasticity dominated fracture mechanisms such as HELP and HESIV, and continuum-based models assuming these mechanisms are lacking [17,28]. Describing damage by these mechanisms in a physically sound way calls for a micromechanics based ductile damage model, such as a Gurson-type model. This type of model aims to describe the full ductile failure process, governed by void growth, nucleation and coalescence.

hydrogen concentration, since more hydrogen results in a faster degradation and accordingly a weaker structural response. Additionally, the introduction of hydrogen into the lattice induces a dilatational strain.

In the context of the HELP mechanism, hydrogen is believed to induce softening of the matrix material, leading to accelerated void coalescence or a change of the failure mode from internal necking to internal shearing coalescence [35]. Hydrogen promoted void growth and coalescence was claimed in numerous experimental studies [36–39]. Furthermore, hydrogen assisted void growth has been observed in numerical studies assuming the HELP mechanism [28,35]. However, such studies are investigating HELP at the level of individual voids by means of unit cell simulations, and do not present a continuum model. In 2019, Yu et al. [28] proposed a hydrogen embrittlement model with damage described by a Gurson model as a first attempt to model the HELP mechanism in a continuum way. The effect of hydrogen was considered by artificially accelerating void growth based on the hydrogen concentration. Unit cell results were compared with a single continuum Gurson element for the derivation of the accelerated void growth parameter. While such comparison is of value since it links the microscopic scale with the continuum scale, they only considered a single element and did not extend the approach towards a full finite element (FE) mesh including hydrogen diffusion.

In the context of the HESIV mechanism where hydrogen promotes the formation of vacancies, the mechanistic effect of hydrogen was related to the increase of void nucleation [7]. Nagumo performed fracture toughness tests on a low carbon ferritic steel, with hydrogen-charged and non-charged specimens. The resulting resistance curves were numerically fitted using a Gurson model. The nucleation parameter increased from 0.02 to 0.035 for the non-charged and hydrogen-charged specimen respectively.

In summary, to our knowledge there is no fully-coupled continuum damage model accounting for the plasticity dominated HE mechanisms. The literature suggests that HE can be modeled in a continuum way by altering either void nucleation according to the HESIV mechanism, or void growth and coalescence according to the HELP mechanism, or a combination hereof.

The present work describes the development of a numerical framework for hydrogen embrittlement simulations at a continuum level, that couples the Complete Gurson Model (CGM) [40] with hydrogen diffusion. The detrimental effect of hydrogen is integrated by artificially accelerating either void growth, void nucleation or void coalescence, depending on the local hydrogen concentration. In this way, the time-dependent macromechanical response in the presence of hydrogen can be simulated, according to the HELP or HESIV mechanisms. Whereas Yu et al. [28] investigated the possibility of using a Gurson model for HELP simulations, the present work aims to deliver a fully coupled micromechanics based model, accounting for both HELP and HESIV. As a case study, a tensile test of a hydrogen-charged notched round bar is simulated, and applications of the different degradation approaches are evaluated.

## 2. Constitutive equations

As already mentioned in the introduction, hydrogen embrittlement simulations require equations describing hydrogen diffusion and mechanical behavior. This section introduces the equations that are hereto adopted in this work. The coupling between the equations will be described in Section 3.

### 2.1. Hydrogen diffusion

In order to assess the detrimental effect of hydrogen on steel, the mechanism as to how hydrogen redistributes throughout the metal must be well understood and equations describing hydrogen transport have to be introduced.

It is well acknowledged that hydrogen atoms inside a metal lattice can either be present at normal interstitial lattice sites or trapped at microstructural defects such as dislocations, grain boundaries, precipitates etc. Since hydrogen diffusion mainly takes place through the transport

of interstitial atoms inside the lattice, trapping sites generally reduce the mobility of hydrogen [30].

For this reason, the total hydrogen concentration  $C$  is typically calculated as the sum of the two populations: lattice hydrogen  $C_L$  and trapped hydrogen  $C_T$  ( $C = C_L + C_T$ ). These two hydrogen populations can be related to the available residing sites in the material [41]:

$$\begin{aligned} C_L &= \beta \theta_L N_L \\ C_T &= \alpha \theta_T N_T \end{aligned} \quad (1)$$

with  $\theta_L$  and  $\theta_T$  being the lattice and trapped occupancy respectively,  $N_L$  and  $N_T$  the density of metal atoms and trapping sites respectively,  $\beta$  the number of interstitial sites per metal atom and  $\alpha$  the number of sites per trap. Assuming tetrahedral occupancy in body centered cubic ferrite,  $\beta$  equals 6. Typically, a single site per trap is assumed, resulting in  $\alpha = 1$  [30,41]. The density of metal atoms  $N_L$  can be evaluated using

$$N_L = \frac{N_A}{V_M} \quad (2)$$

with  $N_A$  the Avogadro constant equal to  $6.022 \times 10^{23} \text{ mol}^{-1}$  and  $V_M$  the molar volume of the host lattice, which is  $7.106 \times 10^{-6} \text{ m}^3/\text{mol}$  for ferrite at room temperature. Evaluating Eq. (2) gives the interstitial lattice site density  $N_L = 8.47 \times 10^{28} \text{ m}^{-3}$ . The trapping density  $N_T$  ( $\text{m}^{-3}$ ) depends on the specific trapping site considered. For defects like grain boundaries or carbides, the trapping densities are often assumed constant throughout the material [30]. However, when dislocations are considered as trapping sites, the trapping density  $N_T$  varies and depends on the local plastic strain  $\epsilon_p$ , since dislocations are generated by plastic strain. Sofronis and McMeeking [41] proposed the following relation for steels based on the experiments of Kumnick and Johnson [42]:

$$\log N_T = 23.26 - 2.33 \exp(-5.5\epsilon_p) \quad (3)$$

Oriani [43] postulated that a local equilibrium exists between the lattice hydrogen  $C_L$  and the trapped hydrogen  $C_T$ , such that:

$$\frac{\theta_T}{1 - \theta_T} = \frac{\theta_L}{1 - \theta_L} K_T \quad (4)$$

with  $K_T = \exp(-E_B/RT)$  the equilibrium constant, where  $E_B$  represents the trap binding energy (J/mol),  $R$  the gas constant (J/(mol K)) and  $T$  the absolute temperature (K). A trap binding energy  $E_B = -60 \text{ kJ/mol}$  was estimated by Kumnick and Johnson [42] and is commonly used in hydrogen embrittlement simulations [27,35,44], although lower values have also been reported for dislocations [30,45].

Mass conservation combined with Oriani's equilibrium results in the well-known model for hydrogen diffusion derived by Krom et al. [44]:

$$\begin{aligned} \frac{C_L + C_T(1 - \theta_T)}{C_L} \frac{\partial C_L}{\partial t} - \nabla \cdot (D_L \nabla C_L) + \nabla \cdot \left( \frac{D_L C_L \bar{V}_H}{RT} \nabla \sigma_h \right) \\ + \alpha \theta_T \frac{dN_T}{d\epsilon_p} \frac{\partial \epsilon_p}{\partial t} = 0 \end{aligned} \quad (5)$$

where  $\bar{V}_H$  equals the partial molar volume of hydrogen ( $\bar{V}_H = 2 \times 10^{-6} \text{ m}^3/\text{mol}$ ). This equation takes into account the balance between lattice and trapped hydrogen, and hydrogen transport driven by the concentration gradient, the hydrostatic stress gradient  $\nabla \sigma_h (= \nabla \sigma_{ii}/3)$  and plastic deformation. The plastic strain rate term was introduced by Krom et al. [44] as an extension of the earlier model of Sofronis and McMeeking [41], to preserve the mass conservation of hydrogen.

### 2.2. Hydrogen damage model

#### 2.2.1. Complete Gurson model

As explained in the introduction, damage will be described by the ductile damage model known as the Complete Gurson Model (CGM) [40,46]. The CGM has been used successfully for predicting fracture in various studies [47–50], and models the complete ductile failure

process, including void growth, nucleation and coalescence [51]. In Gurson-type models, damage is represented by the void volume fraction  $f$ , defined as the ratio of the void volume to a representative volume of the material. Contrary to other Gurson-type models, the critical void volume fraction defining coalescence  $f_c$  is no material constant in the CGM, but instead coalescence is given by the plastic limit load criterion of Thomason [40]. The constitutive yield criterion of the CGM is given by:

$$\phi(\sigma, \bar{\sigma}, f^*) = \left(\frac{\sigma_e}{\bar{\sigma}}\right)^2 + 2q_1 f^* \cosh\left(\frac{3q_2 \sigma_h}{2\bar{\sigma}}\right) - 1 - q_3 f^{*2} = 0 \quad (6)$$

with  $\sigma$  the stress tensor,  $\bar{\sigma}$  the flow stress,  $f^*$  the effective void volume fraction,  $\sigma_e$  the von Mises stress,  $\sigma_h$  the hydrostatic stress, and  $q_1, q_2, q_3$  empirical constants. The effective void volume fraction  $f^*$  was introduced by Tvergaard and Needleman to improve the numerical effect of coalescence, and represents the void volume fraction  $f$  being artificially accelerated upon coalescence [40,52].

An initial void volume fraction  $f_0$  is assigned and void evolution is governed by both the growth of existing voids and the nucleation of new voids ( $\dot{f} = \dot{f}_{\text{growth}} + \dot{f}_{\text{nucleation}}$ ). Void growth is derived from volume conservation upon plastic straining ( $\dot{f}_{\text{growth}} = (1-f)\dot{\epsilon}_{kk}^p$ ) with  $\dot{\epsilon}_{kk}^p$  the trace of the plastic strain rate tensor. Void nucleation is implemented using the strain-controlled approach of Chu and Needleman [53]:

$$\dot{f}_{\text{nucleation}} = \frac{f_N}{s_N \sqrt{2\pi}} \exp\left\{-\frac{1}{2} \left[\frac{\epsilon_p - \epsilon_N}{s_N}\right]^2\right\} \dot{\epsilon}_p \quad (7)$$

with  $f_N$  the void volume fraction of void nucleating particles, and  $s_N$  and  $\epsilon_N$  the standard deviation and the mean of nucleating strain respectively. All load-carrying capacity has disappeared when  $f$  reaches the final void volume fraction  $f_f$ .

The physical void coalescence process can occur in different modes, depending on the loading conditions and microstructural features [51, 54]. The most common mode is coalescence by internal necking of the ligament between neighboring voids. A second mode is coalescence by internal shearing, where micro shear bands are formed inclined to the main loading direction, joining neighboring voids. The internal necking mechanism is dominant at high stress triaxiality, while the internal shearing coalescence is more observed in low stress triaxiality states [54]. The triaxiality value defining the transition between internal shearing and internal necking is uncertain. Kiran et al. [55] reported the inapplicability of the Gurson model for triaxiality values below 0.3 due to shear localization. Danas et al. [56] mentioned that the transition value of triaxiality is around 0.7–0.8, based on fracture surfaces of hot-rolled medium-strength steel. In the context of modeling ductile failure, a micromechanics-based coalescence model for internal necking was developed by Thomason [57] and is implemented in the CGM as follows:

$$\sigma_1 = \bar{\sigma} \left( \alpha^T \left( \frac{1}{r} - 1 \right)^2 + \frac{\beta^T}{\sqrt{r}} \right) \left( 1 - \frac{\pi}{4} r^2 \right) \quad (8)$$

with  $\sigma_1$  the maximum principal stress,  $r$  the void space ratio defined as  $r = \sqrt[3]{3f/4\pi}/(\sqrt{e^{\epsilon_2} + \epsilon_3}/2)$ ,  $\epsilon_i$  the principal strains,  $\alpha^T = 0.12 + 1.68n$  and  $\beta^T = 1.2$  numerical constants fitted by Zhang [40] (note that the factor 4 in Eq. (8) was missing in Zhang et al.'s original paper due to a typographic error [40]). The strain hardening exponent  $n$  is determined according to the equation  $\sigma/\sigma_0 = (1 + E\epsilon_p/\sigma_0)^n$ , describing the true stress–true strain behavior of the material with  $\sigma_0$  the yield strength, and  $E$  the Young's modulus. When  $\sigma_1$  reaches the value of the right hand side of Eq. (8), coalescence has occurred and  $f_c$  is equated to the corresponding void volume fraction.

In total, the complete Gurson model comprises eight parameters ( $\epsilon_N, s_N, f_N; f_0, f_f; q_1, q_2, q_3$ ) requiring calibration for a given material. In practice, these parameters are often selected based on a combination of literature data and the fitting of experimental and numerical force versus displacement curves [58].

### 2.2.2. Degradation due to hydrogen

The complete Gurson model describes void growth, nucleation and coalescence. Physically, each of these three processes can be accelerated due to hydrogen, depending on the assumed HE mechanism (see Section 1).

The effect of hydrogen on void growth and coalescence has been assessed with numerical simulations using a unit cell containing a void [35,59–61]. In these studies a spherical void was modeled, and the matrix material was softened locally, based on the local hydrogen concentration. The use of unit cells serves as a first step towards improved insight in hydrogen promoted void growth and coalescence [61]. This knowledge about void behavior can then be transferred to a continuum damage model, such as Gurson-type models.

An approach to associate the unit cells with a Gurson-type model was proposed by Yu et al. [28]. The micromechanical background of the Gurson model is partially discarded, and  $f$  is exclusively seen as a parameter describing damage, rather than representing the actual void volume fraction. In their study, the void growth  $\dot{f}$  is made dependent on the hydrogen concentration, and accelerated hydrogen failure occurs. Due to lack of further information regarding the degrading hydrogen effect, Yu proposed a linear scaling function and numerically calibrated the degradation factor by comparing unit cell results with single-element simulations. The following formulation was obtained:

$$\dot{f}_{\text{growth}}(C_L) = \dot{f}_{\text{growth}_0} (1 + 0.16C_L) \quad (9)$$

where  $\dot{f}_{\text{growth}_0}$  signifies the void growth calculated without any hydrogen. No void nucleation term was employed in their model. A limitation of this equation is that it was calibrated using simulations with a specific set of parameters exclusively. Comparison with experimental data is lacking, and assumptions regarding hydrogen softening and trapping were required. Furthermore, by increasing the void growth, the conservation of volume principle used to derive  $\dot{f}_{\text{growth}_0}$  is no longer fulfilled. Finally, coalescence was described with the parameter  $f_c$ , contrary to the CGM, which models coalescence using Thomason's criterion.

Without further elaboration on the potential limitations resulting from the assumptions above, it suffices for this study that Eq. (9) does allow to evaluate the ability to implement hydrogen assisted degradation into our developed model. Similarly to Yu, linear dependence of hydrogen concentration is used in the current study, but Eq. (9) was slightly adapted for the following reasons. According to Jemblie et al. [30], no consensus is obtained as to whether hydrogen damage should be dependent on the lattice concentration, on the trapped concentration or on both. Besides, the process of accelerated void nucleation due to hydrogen is also implemented. Accordingly, the accelerated void volume fraction due to hydrogen is generically implemented in our numerical framework as follows, potentially taking into account both HELP and HESIV:

$$\begin{aligned} \dot{f}_{\text{growth}}(C_L, C_T) &= \dot{f}_{\text{growth}_0} (1 + k_{g,L} C_L + k_{g,T} C_T) \\ \dot{f}_{\text{nucleation}}(C_L, C_T) &= \dot{f}_{\text{nucleation}_0} (1 + k_{n,L} C_L + k_{n,T} C_T) \end{aligned} \quad (10)$$

where  $k_{g,L}, k_{g,T}, k_{n,L}$  and  $k_{n,T}$  are degradation factors requiring calibration ( $\text{wppm}^{-1}$ ), and the hydrogen concentrations  $C_L$  and  $C_T$  are expressed in weight parts per million (wppm). It is clear that Yu et al.'s original equation can be easily obtained from Eq. (10) by setting  $k_{g,L} = 0.16$ ,  $k_{g,T} = 0$  and deactivating void nucleation.

Other than accelerating the void growth and nucleation processes due to hydrogen, the coalescence criterion may also be adjusted for taking hydrogen into account, based on the following reasoning. When modeling HELP in unit cell simulations, the flow stress in the matrix material is assumed to decrease with hydrogen concentration. Following formulation is most widely adopted [28], consisting of a linearly decreasing stage and a constant stage:

$$\bar{\sigma}_H(C_L) = \begin{cases} \left[ \left( \xi - 1 \right) \frac{C_L}{C_0^L} + 1 \right] \bar{\sigma} & \bar{\sigma}_H(C_L) > \xi \bar{\sigma} \\ \xi \bar{\sigma} & \bar{\sigma}_H(C_L) \leq \xi \bar{\sigma} \end{cases} \quad (11)$$



with  $\bar{\sigma}_H$  the flow stress reduced by hydrogen,  $\xi$  the hydrogen softening parameter,  $C_L^0$  the initial lattice hydrogen concentration and  $\zeta$  a fraction that determines a lower bound value of flow stress. Such type of softening law has been successfully used in modeling accelerated damage in unit cells [28,35,61], however direct implementation of this law in a yield criterion on a continuum basis (such as Eq. (6)) is unsound, as demonstrated by Yu et al. [28]. It is the local hydrogen softening at the ligament between voids that is responsible for accelerated failure, rather than global hydrogen softening across the whole element. Since in a Gurson model, a certain flow stress is associated with an element implicitly containing a void, it is not possible to soften the ligament only locally. For this reason, in our framework, hydrogen softening is implemented into Thomason's coalescence criterion only, by substituting  $\bar{\sigma}$  in Eq. (8) with  $\bar{\sigma}_H$  from Eq. (11). In this way, coalescence is accelerated as claimed by the HELP mechanism.

Different degradation factors are introduced to allow for hydrogen assisted degradation. Possibilities to calibrate these factors include comparison with unit cell simulations, comparison with hydrogen-charged mechanical tests, and identification using micromechanical developments.

In summary, the developed framework allows to accelerate either void growth, nucleation or coalescence, or a combination hereof. Even though hydrogen might change the failure mode from internal necking to internal shearing under certain conditions [35], a coalescence criterion describing internal shearing is not implemented yet. This could be addressed in a future extension in an effort to deliver a complete numerical framework accounting for all conditions.

### 3. Implementation into finite element analysis

The full coupling of hydrogen diffusion with damage evolution has been implemented into Abaqus (version 2019) using three user subroutines. Fig. 1 illustrates the sequential calling of the user subroutines, together with the storage and extraction of data in solution-dependent variables (SDV), common variables and the .fil result files. First, user subroutines UMAT and UMATHT are called for each integration point, computing the mechanical behavior and hydrogen concentration respectively. If the solution does not converge according to the Abaqus built-in convergence criteria [62], a new iteration is attempted or the time increment is automatically reduced. At the end of the increment, the user subroutine URDFIL is called and the hydrostatic pressure gradient of the converged increment is calculated.

#### 3.1. Hydrogen diffusion (UMATHT)

To model hydrogen diffusion in a numerical framework, the analogy between heat transfer and mass diffusion equations is widely used [19, 26,27,63], bearing in mind that thermal constitutive behavior can be user customized in Abaqus using a UMATHT [62]. The heat transfer equation is given by:

$$\rho \frac{\partial U}{\partial t} + \nabla \cdot \mathbf{J}_q = q \quad (12)$$

with  $\rho$  the mass density,  $U$  the internal thermal energy,  $\mathbf{J}_q$  the heat flux vector and  $q$  the heat supplied externally into the body. By defining the relation between the internal thermal energy  $U$  and the temperature  $T$ , a thermal analysis can be performed. By setting  $\rho \equiv 1$  and  $q \equiv 0$ , the heat transfer equation (Eq. (12)) is equated with the hydrogen diffusion equation (Eq. (5)) by stating that:

$$\begin{aligned} \frac{\partial U}{\partial t} &\equiv \frac{C_L + C_T(1 - \theta_T)}{C_L} \frac{\partial C_L}{\partial t} + \alpha \theta_T \frac{dN_T}{d\epsilon_p} \frac{\partial \epsilon_p}{\partial t} \\ \mathbf{J}_q &\equiv -D_L \nabla C_L + \frac{D_L C_L \bar{V}_H}{RT} \nabla \sigma_h \end{aligned} \quad (13)$$

Yet another analogy is employed. Since  $\nabla C_L$  is required for the definition of the constitutive equations (see Eq. (13)), the "temperature"  $T$  is replaced by the unknown lattice hydrogen concentration:  $T \equiv C_L$ .

Because Abaqus provides the spatial gradients of the temperature  $\nabla T$ , the lattice hydrogen concentration gradient  $\nabla C_L$  can be used in the definition of the flux vector  $\mathbf{J}_q$ , without the explicit calculation hereof. The corresponding trapped hydrogen concentration  $C_T$  can then be computed using Oriani's equilibrium (Eq. (4)).

Eq. (13) requires an advanced thermal material model in Abaqus. Accordingly, a UMATHT user subroutine is written, which requires the definition of following variables:  $U$ ,  $\partial U / \partial C_L$ ,  $\partial U / \partial \nabla C_L$ ,  $\mathbf{J}_q$ ,  $\partial \mathbf{J}_q / \partial C_L$ ,  $\partial \mathbf{J}_q / \partial \nabla C_L$  [62] (where  $T$  has been substituted by  $C_L$ ). Transforming Eq. (13) into finite difference approximations and further derivation results in:

$$\begin{aligned} U(t + \Delta t) &= U(t) + \frac{C_L + C_T(1 - \theta_T)}{C_L} \Delta C_L + \alpha \theta_T \frac{dN_T}{d\epsilon_p} \Delta \epsilon_p \\ \frac{\partial U}{\partial C_L} &= \frac{C_L + C_T(1 - \theta_T)}{C_L} \\ \frac{\partial U}{\partial \nabla C_L} &= \mathbf{0} \\ \frac{\partial \mathbf{J}_q}{\partial C_L} &= \frac{D_L \bar{V}_H}{RT} \nabla \sigma_h \\ \frac{\partial \mathbf{J}_q}{\partial \nabla C_L} &= -D_L \mathbf{I} \end{aligned} \quad (14)$$

where the definition of the flux vector  $\mathbf{J}_q$  is already given by Eq. (13).

Note that the implementation of Eq. (14) requires the values of two mechanical quantities besides the hydrogen-related values, namely the local hydrostatic stress gradient  $\nabla \sigma_h$  and the equivalent plastic strain increment  $\Delta \epsilon_p$ . The requirement of these quantities necessitates coupling between the diffusion analysis and the stress analysis.

The correct implementation of the aforementioned hydrogen diffusion equations (Eqs. (13) and (14)) has been verified by modeling a modified boundary layer model (Fig. 2a). This model has been commonly used to examine the effect of the stress field surrounding a crack on the plastic zone ahead of the crack tip [64]. A modified boundary layer model describes a two-dimensional disc containing a crack, loaded under plane strain conditions. More details regarding this type of geometry can be found in [65]. In this study, a displacement field  $u_i$  is applied at the disc boundary corresponding to the theoretical displacement field associated with a stress intensity factor of  $K_I = 89.2 \text{ MPa}\sqrt{\text{m}}$ . Recalling that the developed material model is based on three-dimensional brick elements, two-dimensional plane strain conditions were achieved by simulating a single layer of elements and applying out-of-plane symmetry boundary conditions to the front and back face. Hydrogen diffusion in the same configuration was simulated by Krom et al. [44]; their results are used as a benchmark in this study. An initial lattice hydrogen concentration  $C_{L,0}$  is applied throughout the specimen, and the boundary of the model is set at a constant lattice hydrogen concentration  $C_{L,0}$ . The displacement  $u_i$  is applied over various loading times, and numerical parameters are chosen the same as in Krom et al. [44]. The comparison is presented in Fig. 2(b) where the normalized lattice hydrogen concentration  $C_L/C_{L,0}$  is set out against the normalized distance to the crack tip  $R/b$  for different loading times. An excellent agreement can be observed. The normalized trapped hydrogen  $C_T/C_{L,0}$  was also calculated and similarly agrees with the results reported in [44].

#### 3.2. Complete Gurson Model (UMAT)

The Abaqus implementation of the CGM is done through a UMAT user subroutine, which defines the mechanical constitutive behavior of the material [62]. This UMAT is based on source code developed by Zhang et al. [40]. It also contains the mechanical degradation due to hydrogen (Eqs. (10) and (11)). Void evolution is monitored using solution-dependent state variables. Also the local increment in equivalent plastic strain  $\Delta \epsilon_p$  is stored in a solution-dependent state variable, such that the UMATHT user subroutine for calculating hydrogen diffusion is able to use this quantity (recall Eq. (14)). Since the UMAT is

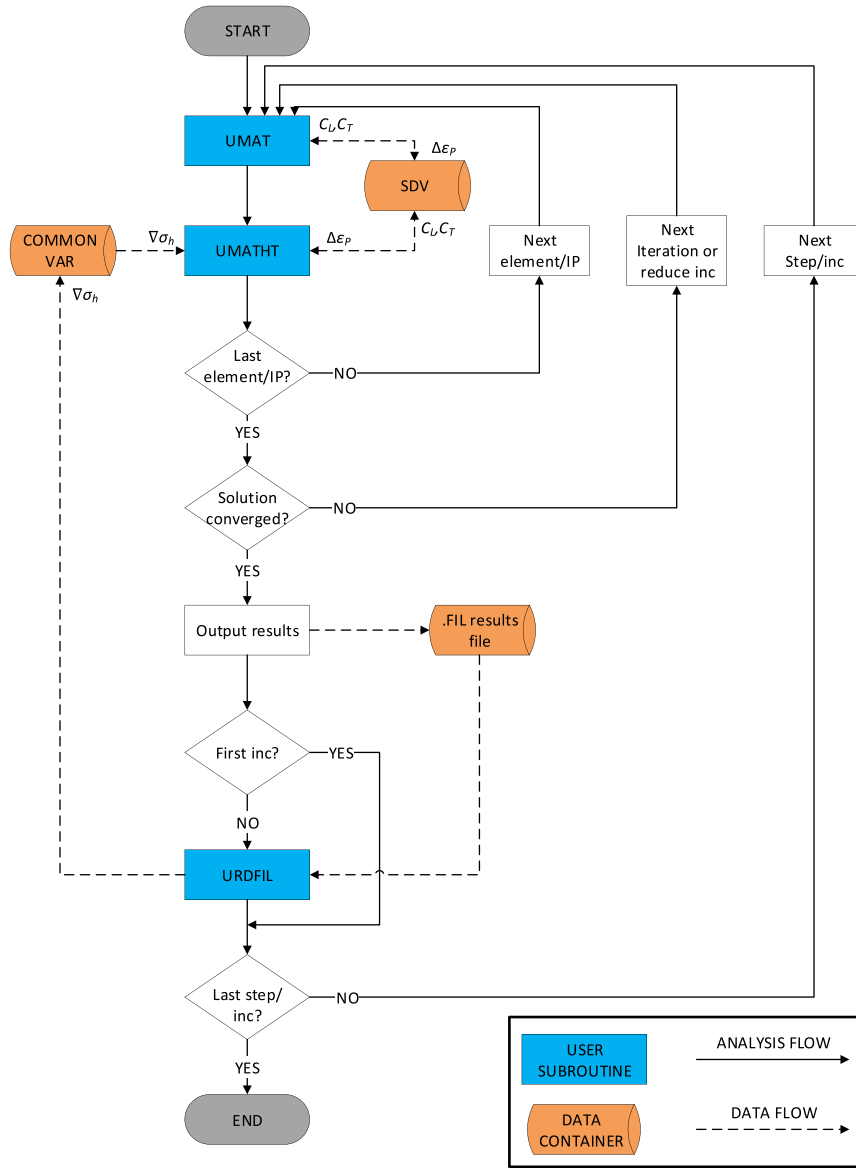


Fig. 1. Flowchart sequence user subroutine calls (IP = integration point, SDV = solution-dependent variables, inc = increment).

called before the UMATHT at every integration point [62] (see Fig. 1), the current plastic strain increment is employed. This is contrary to the approach developed by Gobbi et al. [27], where the preceding  $\Delta\epsilon_p$  is used. However, it was argued in their paper that the associated error with this forward approach is negligible for small  $\Delta t$ .

### 3.3. Calculation of the hydrostatic stress gradient (URDFIL)

The hydrostatic stress gradient  $\nabla\sigma_h$  is required for the computation of the local hydrogen concentration. The calculation is not straightforward, and involves the extraction of the nodal hydrostatic stresses and coordinates, and the differentiation of the shape functions  $N^i$ .

In the current framework, three-dimensional 8-noded coupled temperature–displacement brick elements (C3D8T) are employed. These elements have 8 integration points, at which the stresses are calculated during the analysis. However for the gradient calculation, stresses at the nodes are preferred. The argumentation hereto is that calculating the gradient based on integration points could result in discontinuity between the elements, thus affecting numerical stability [63]. As such, the gradient at a particular integration point is approximated using the nodal hydrostatic stresses of the corresponding

element  $\sigma_{h_i}^N$  and the derivatives of the shape functions at this point. Accordingly, the hydrostatic stress gradient is computed as follows:

$$\begin{aligned}\frac{\partial\sigma_h}{\partial x} &= \sum_{i=1}^8 \frac{\partial N^i}{\partial x} \sigma_{h_i}^N \\ \frac{\partial\sigma_h}{\partial y} &= \sum_{i=1}^8 \frac{\partial N^i}{\partial y} \sigma_{h_i}^N \\ \frac{\partial\sigma_h}{\partial z} &= \sum_{i=1}^8 \frac{\partial N^i}{\partial z} \sigma_{h_i}^N\end{aligned}\quad (15)$$

The derivatives of the shape functions in the global coordinate system  $(x, y, z)$  are calculated using the derivatives in a local coordinate system  $(\xi', \eta', \zeta')$ :

$$\begin{bmatrix} \frac{\partial N}{\partial x} \\ \frac{\partial N}{\partial y} \\ \frac{\partial N}{\partial z} \end{bmatrix} = [J]^{-1} \begin{bmatrix} \frac{\partial N}{\partial \xi'} \\ \frac{\partial N}{\partial \eta'} \\ \frac{\partial N}{\partial \zeta'} \end{bmatrix}\quad (16)$$

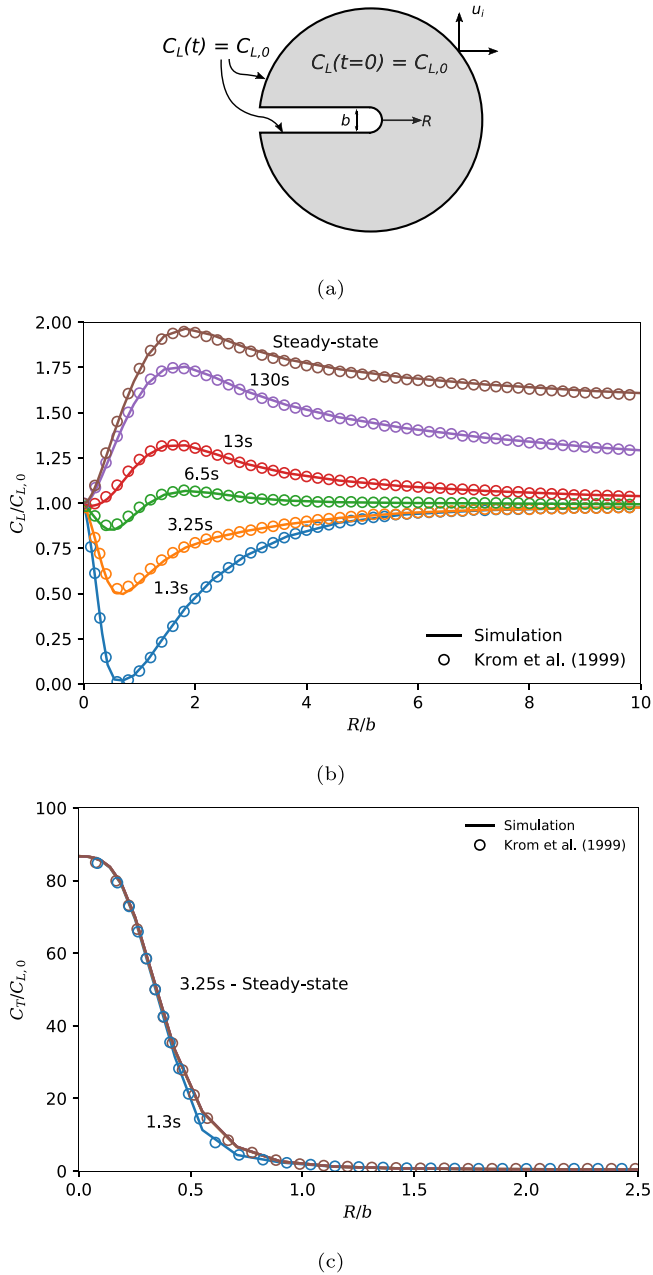


**Fig. 2.** (a) Schematic of the geometry and boundary conditions of a modified boundary layer model, (b) the normalized lattice  $C_L/C_{L,0}$  and (c) normalized trapped  $C_T/C_{L,0}$  hydrogen concentration near the crack tip in a loaded modified boundary layer model for different loading times.

Source: A good agreement with the published results of Krom et al. [44] is obtained.

where  $[J]$  represents the Jacobian matrix, consisting of the derivatives of the global coordinates with respect to the local coordinates:

$$[J] = \begin{bmatrix} \frac{\partial x}{\partial \xi^i} & \frac{\partial y}{\partial \xi^i} & \frac{\partial z}{\partial \xi^i} \\ \frac{\partial x}{\partial \eta^i} & \frac{\partial y}{\partial \eta^i} & \frac{\partial z}{\partial \eta^i} \\ \frac{\partial x}{\partial \zeta^i} & \frac{\partial y}{\partial \zeta^i} & \frac{\partial z}{\partial \zeta^i} \end{bmatrix} = \begin{bmatrix} \sum_{i=1}^8 \frac{\partial N^i}{\partial \xi^i} x_i^N & \sum_{i=1}^8 \frac{\partial N^i}{\partial \xi^i} y_i^N & \sum_{i=1}^8 \frac{\partial N^i}{\partial \xi^i} z_i^N \\ \sum_{i=1}^8 \frac{\partial N^i}{\partial \eta^i} x_i^N & \sum_{i=1}^8 \frac{\partial N^i}{\partial \eta^i} y_i^N & \sum_{i=1}^8 \frac{\partial N^i}{\partial \eta^i} z_i^N \\ \sum_{i=1}^8 \frac{\partial N^i}{\partial \zeta^i} x_i^N & \sum_{i=1}^8 \frac{\partial N^i}{\partial \zeta^i} y_i^N & \sum_{i=1}^8 \frac{\partial N^i}{\partial \zeta^i} z_i^N \end{bmatrix} \quad (17)$$

with  $(x_i^N, y_i^N, z_i^N)$  the coordinates of node  $i$ .

Previous equations indicated the requirement of nodal coordinates  $(x_i^N, y_i^N, z_i^N)$  and nodal hydrostatic stresses  $\sigma_{h_i}^N$ . Nodal coordinates and nodal hydrostatic stresses are stored in a .fil file, together with the

connectivity matrix containing the nodes for each element. This file is then read by the URDFIL user subroutine as indicated in Fig. 1.

The URDFIL user subroutine evaluates preceding equations for each integration point, and the hydrostatic stress gradients are computed for the converged increment. The stress gradients  $\nabla \sigma_h$  are then stored using a FORTRAN common block, such that these can be employed in the computation of the hydrogen concentration in the UMATHT subroutine. Note that the Jacobian matrix  $[J]$  is calculated for each converged increment, unlike the implementation by Gobbi et al. [27] where the calculation of  $[J]$  is done prior to analysis. They argued that this approach is valid for small displacements. However, since large deformations are expected if ductile rupture is the failing process [66], this approach was not adopted. Furthermore, since URDFIL is only called at the end of a converged increment, the hydrostatic stress gradient of the previous increment is used for the calculation of the hydrogen concentration. For this reason, the time increment should be chosen small enough.

The hydrostatic stress gradient calculation is verified by comparing the calculated quantities with a finite difference approximation of the derivative of the hydrostatic stresses along a path.

#### 4. Effects of discretization parameters on numerical accuracy

As an essential step to use the numerical framework as a tool to predict hydrogen embrittlement, the sensitivity of the results to numerical discretization parameters such as the time increment and the element size must be understood.

For that goal, the present work simulates tensile tests on hydrogenated notched round bar specimens. This type of geometry is well suited to study ductile failure [67], and is therefore commonly used for the determination of local damage model parameters [51], which makes it an interesting geometry to assess the hydrogen effect. The notch induces a high triaxial stress state and a high hydrostatic stress gradient inside the specimen, thus attracting hydrogen. By varying the ratio of the notch radius to the specimen diameter, triaxiality values up to 2 can be obtained [51,68] and the hydrogen effect at different levels of stress triaxiality can be assessed. Fig. 3 shows the dimensions and the boundary conditions of the notched round bar, together with one of the meshes employed. One quarter of the specimen is modeled with corresponding symmetry boundary conditions. A uniform initial lattice hydrogen concentration  $C_{L,0}$  is assigned. Upon the start of loading, the hydrogen concentration at the boundary is set to zero, allowing lattice hydrogen to effuse out of the specimen. This represents an idealization of the contact with air during a tensile test using a hydrogen pre-charged specimen. Nonlinear geometric effects were activated, to account for large deformations. Element deletion was activated.

Table 1 contains the relevant parameters employed during the simulations, and Fig. 4 presents the adopted true stress versus true plastic strain curve. The plastic stress-strain material behavior and CGM parameters were determined by comparing numerical simulations with experimental tensile test results, using an API 5L [69] X70 pipeline steel free of hydrogen. A nominal triaxiality value of 1.6 was obtained at the center of the model. In the simulations, a displacement of 2 mm was applied during a total time of 2400 s, corresponding to a displacement rate of  $8.33 \times 10^{-4}$  mm/s. A diffusion coefficient  $D_L = 1.5 \times 10^{-4}$  mm<sup>2</sup>/s was adopted, relevant to pipeline steel.

To investigate the effect of element size and time increment, four element sizes  $l_c$  (0.05 mm, 0.1 mm, 0.2 mm, 0.4 mm) and five time increments (1 s, 6 s, 24 s, 60 s, 120 s) were targeted. First, the effects on the diffusion and degradation aspects are investigated separately, aiming to provide insight in the functioning of the independent modules (Sections 4.1 and 4.2). Thereafter, coupled effects are characterized, with the purpose of determining guidelines to use the framework such that the simulations are both numerically trustworthy and computationally efficient (Section 4.3).

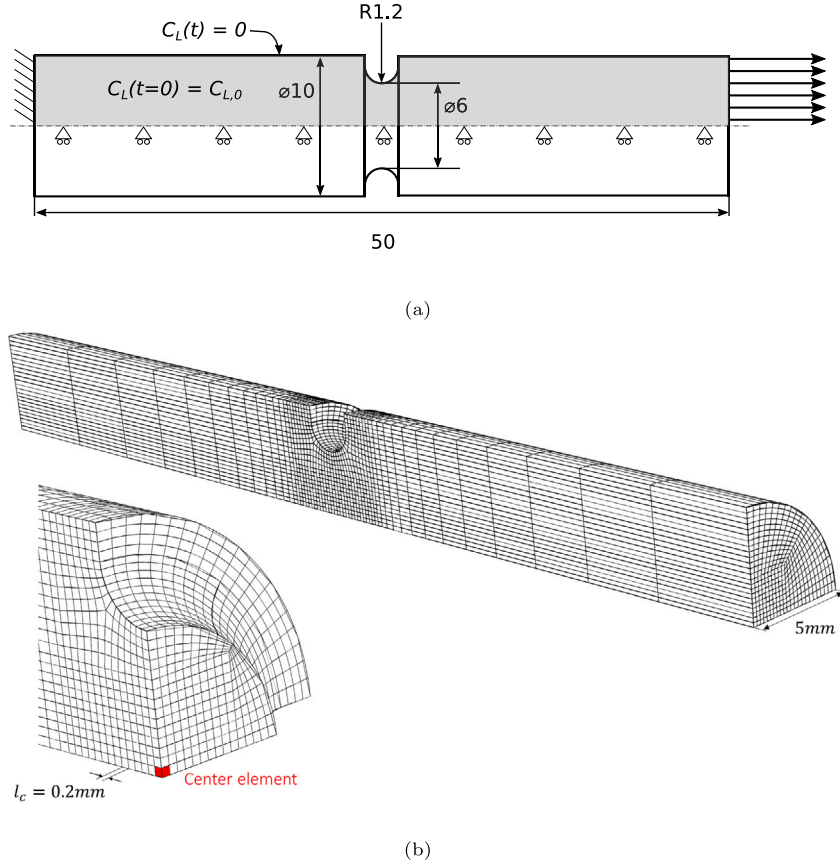


Fig. 3. (a) Geometry of the notched round bar tensile specimen (dimensions in mm), (b) the finite element mesh employed, with a detail of the notched zone.

Table 1

Material properties employed during simulations.

Property	Value
Mechanical and ductile damage	
$E$	207 000 MPa
$\nu$	0.3
$\epsilon_N$	0.3
$s_N$	0.1
$f_N$	0.013
$f_0$	0.00012
$f_f$	0.27
$q_1$	1.42
$q_2$	0.96
$q_3$	2.03
Hydrogen diffusion	
$C_{L,0}$	1.0 wppm = $4.70 \times 10^{24} \text{ m}^{-3}$
$E_B$	-60 kJ/mol
$N_L$	$8.47 \times 10^{28} \text{ m}^{-3}$
$T$	300 K
$\alpha$	1
$\beta$	6

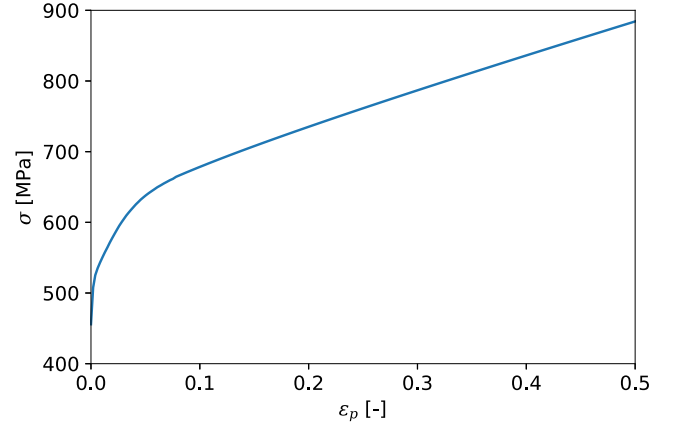


Fig. 4. True stress  $\sigma$  versus true plastic strain  $\epsilon_p$  employed for the simulations. The data have been obtained from tensile experiments on an X70 pipeline steel.

#### 4.1. Hydrogen diffusion

To investigate the effects of element size and time increment on hydrogen diffusion separately, regular  $J_2$ -plasticity was implemented, i.e. the damage and degradation modules were kept inactive. First, five different time increments ( $\Delta t = 1\text{ s}; 6\text{ s}; 24\text{ s}; 60\text{ s}; 120\text{ s}$ ) were simulated with a fixed element size ( $l_c = 0.2\text{ mm}$ ). Further, four different element sizes at the notched region ( $l_c = 0.05\text{ mm}; 0.1\text{ mm}; 0.2\text{ mm}; 0.4\text{ mm}$ ) were employed with a fixed time increment ( $\Delta t = 6\text{ s}$ ). Fig. 5 plots the hydrogen concentration at the element touching the specimen center (see Fig. 3) as a function of time. The increased hydrogen concentration

due to stress-assisted diffusion is apparent. Note that the hydrogen concentration at the center element converges for both smaller element sizes and smaller time increments.

Both a mesh and increment dependency of the diffusion results are expected for the following reasons. The diffusion equation includes the hydrostatic stress gradient  $\nabla\sigma_h$ . Consequently, an altered mesh causes an altered hydrostatic stress field, accordingly resulting in changed hydrogen concentrations. Moreover, the dependence on the hydrostatic stress gradients is implemented in a forward way: the previously converged  $(\nabla\sigma_h)_{i-1}$  is used for determining the current hydrogen concentration  $(C_L)_i$ . This explains the seemingly delayed response of the hydrogen concentration for large increments (see Fig. 5b).



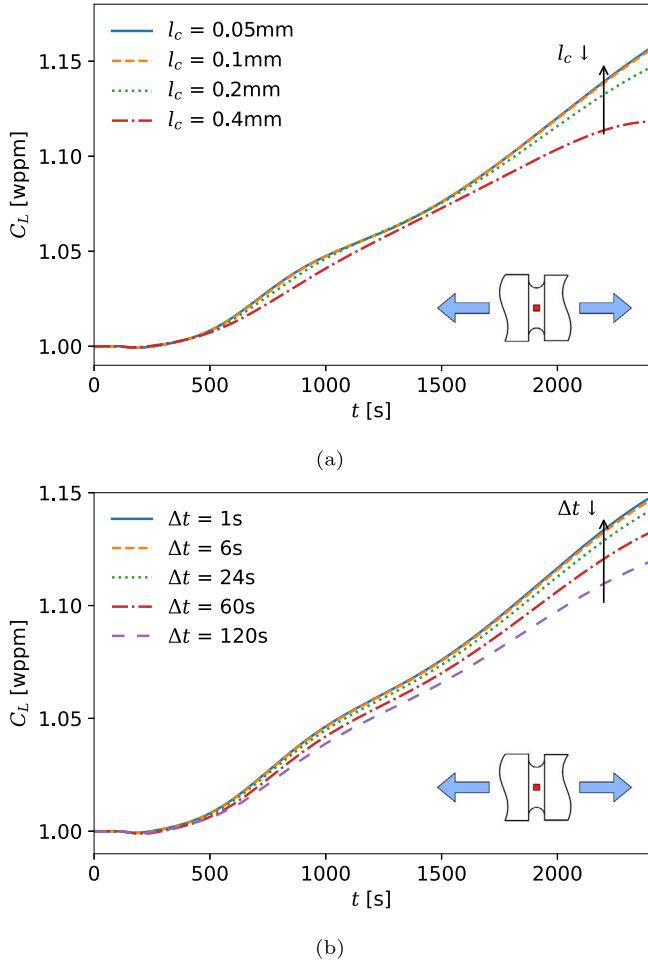


Fig. 5. Hydrogen concentration at the center element for various (a) element sizes  $l_c$  and (b) time increments  $\Delta t$  ( $D_L = 1.5 \times 10^{-4} \text{ mm}^2/\text{s}$ ). Convergence is observed for decreasing element sizes and time increments.

Note that the hydrogen concentration near the end does not represent a physically realistic value, because the model comprises excessively unrealistic deformations due to the inactivation of damage. For example note that a plastic strain  $\epsilon_p$  of 0.95 in the center is obtained at the end of the simulation.

#### 4.2. Damage

The effect of increment and element size on the outputs of the complete Gurson model is investigated using a parametric study with the same parameters as those in Section 4.1. Hydrogen assisted degradation has been kept inactive, thus simulating notched tensile tests in absence of hydrogen. Fig. 6 gives the force ( $F$ ) - elongation ( $\Delta L$ ) curves for various parameter values. Damage initiation occurs at the center element and propagates radially outwards. To relate the global load-elongation curve to local damage, the start of coalescence ( $f = f_c$ ) and complete failure ( $f = f_f$ ) of the center element are displayed with a circle and a star symbol respectively. No convergence of the simulated force-elongation curves is observed for the different element sizes (Fig. 6a). Alternatively, the effect of different time increments on these curves is limited and convergence is observed for smaller increments (Fig. 6b). Note that it was not possible to perform the simulation with the smallest element size ( $l_c = 0.05$  mm) completely. However, this particular element size is small compared to simulations using the CGM found in literature and therefore less relevant [70].

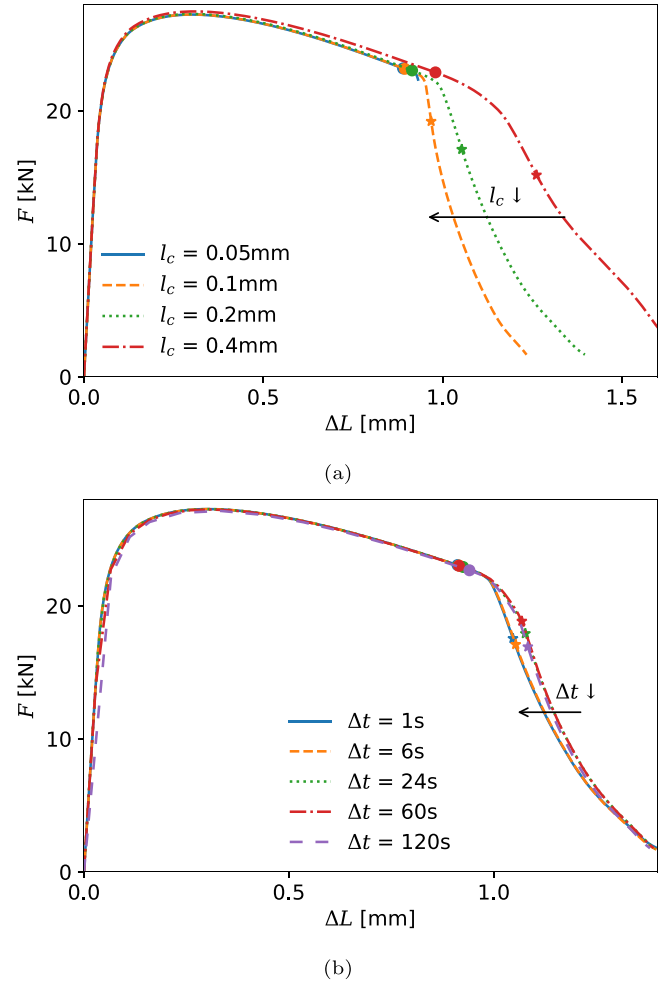


Fig. 6. Force versus elongation for various (a) element sizes  $l_c$  and (b) time increments  $\Delta t$  without hydrogen assisted degradation. The start of coalescence, and the occurrence of complete failure of the center element are represented by a circle and a star symbol respectively. While convergence occurs for decreasing time increments, the element size dependency is not converging.

Both the increment and the element size dependency of local micromechanical damage models have been well investigated [40,71,72]. In particular, the non-converging element size dependency is known and seen as a drawback of the use of local damage models for predicting failure. The cause hereof is the localization of damage in a single layer of elements. In practice, this problem can be overcome by using the same element size during both the calibration of the model parameters as well as the following simulations [66], or by making use of a more advanced so-called ‘non-local’ damage model [73]. For reasons of simplicity, the former approach is adopted in the present study, and an element size of 0.2 mm is chosen.

#### 4.3. Coupled effects

The effects of increment and element size on the fully coupled diffusion-degradation-damage model are evaluated. Degradation according to Yu et al. [28] is employed, i.e.  $k_{g,L} = 0.16 \text{ wppm}^{-1}$ . Fig. 7 presents the force-elongation curves for various element sizes and time increments. The curves without degradation are shown in gray for comparison. It is apparent that the degradation due to hydrogen by accelerating the void volume fraction leads to the experimentally observed macromechanical ductility loss. However, it is striking that the effect of element size is larger than the effect of degradation,

for this particular degradation factor. This observation reaffirms the importance of choosing a fixed element size for the calibration of the hydrogen-free damage model parameters ( $\epsilon_N$ ,  $s_N$ ,  $f_N$ ;  $f_0$ ,  $f_f$ ;  $q_1$ ,  $q_2$ ,  $q_3$ ) and subsequent simulations adopting these parameters.

The effects of discretization parameters identified in Sections 4.1 and 4.2 also appear in the fully coupled simulations. Similar to Fig. 6, a non-converging effect of the element size on the force–elongation curve is observed in Fig. 7. Furthermore, note that the two smaller element sizes ( $l_c = 0.05$  mm and 0.1 mm) cause analysis convergence problems. Again, as already mentioned in Section 4.2, these element sizes are less relevant for damage modeling using a local damage model.

Regarding the time increments, converging results can be observed for smaller increments, as could be expected from the separate investigations of the diffusion and damage module.

Based on the preceding observations, a preliminary study is advised when employing the framework with a new geometry, to determine adequate discretization parameters. The effect of these parameters on the accuracy and computation time can be assessed from the separate modules. A diffusion-only analysis is suggested with different element sizes to analyze the convergence of the hydrogen concentration. Accordingly, a certain element size is selected. Following, separate diffusion and damage analyses with different time increments and the adopted element size are proposed. Thus, an adequate time increment is chosen where both analyses are converged.

By following the aforementioned procedure in this particular example, an element size  $l_c = 0.2$  mm and a time increment  $\Delta t = 6$  s are adopted for the remainder of this study. The maximum local hydrogen concentration achieved is around 1.05 wppm at the center element, after which failure occurs.

## 5. Effect of hydrogen assisted degradation and diffusion on ductility

### 5.1. Hydrogen assisted degradation

With the aim of exploring the ability of the developed model to describe hydrogen assisted degradation, the effect of hydrogen on each of the three processes governing ductile damage – void nucleation, growth and coalescence – is activated separately. As explained in Section 2.2.2, hydrogen accelerated void nucleation shows the mechanistic effect of the HESIV mechanism, while hydrogen accelerated void growth or coalescence is associated with the HELP mechanism. In the current work, hydrogen assisted degradation due to trapped hydrogen is not considered, since the trapped hydrogen concentration  $C_T$  is much smaller than the lattice hydrogen concentration  $C_L$  for the parameters employed ( $C_T = 3.7 \times 10^{-2}$  wppm for a plastic strain  $\epsilon_p = 1.0$ ). Furthermore, a lattice diffusion coefficient  $D_L = 1.5 \times 10^{-4}$  mm<sup>2</sup>/s is assumed. Other employed model parameters can be found in Table 1.

By increasing the degradation factor  $k_{g,L}$ , void growth is accelerated and larger ductility losses are obtained, as expected (Fig. 8a). Looking at the fully completed simulations, the model succeeds in describing a substantial ductility loss due to hydrogen. It should however be noted that large degradation factors are required. With  $k_{g,L} = 0.16$  wppm<sup>-1</sup>, as adopted by Yu, only a limited ductility loss due to hydrogen is obtained, contrary to experimental values reported in literature for tensile tests on hydrogen charged notched round bar specimens [74–76]. The evolution of the local void volume fraction  $f$  versus the local plastic strain  $\epsilon_p$  in the center element shows the accelerated failure due to the presence of hydrogen (Fig. 8b): a lower plastic strain is reached upon complete failure. The stress triaxiality at the center element versus the plastic strain is also presented (Fig. 8c). The data is displayed until the start of coalescence, since stress values in a discrete element are believed to be irrelevant after damage localization. The fast increase in triaxiality value for the largest degradation factors is also related to damage localization at the center.

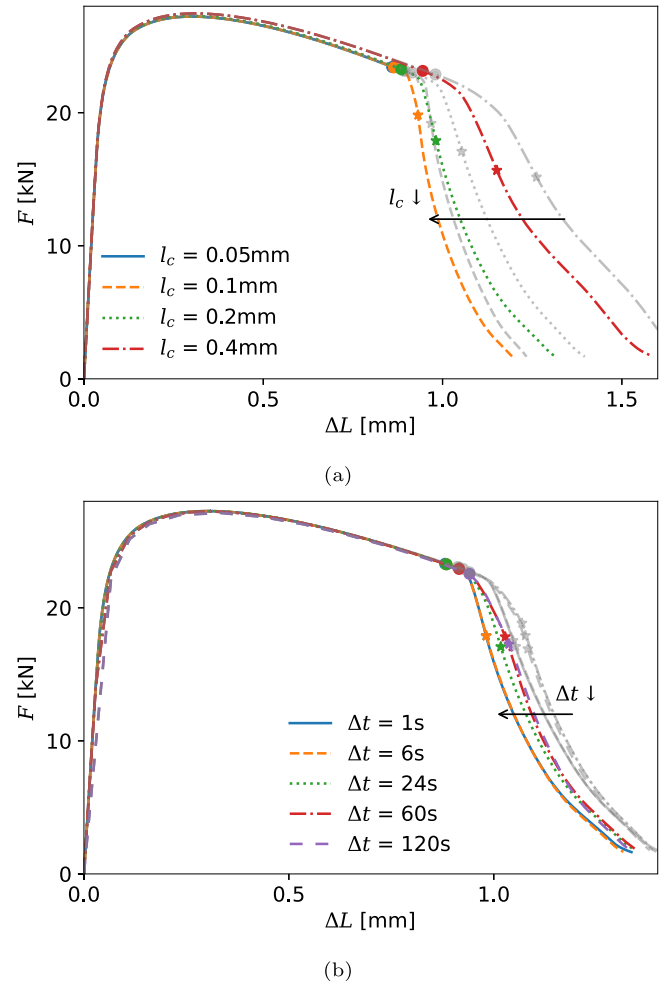


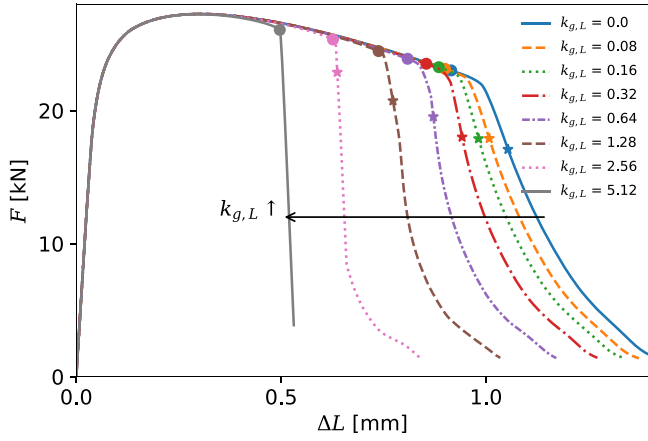
Fig. 7. Force versus elongation for various (a) element sizes  $l_c$  and (b) time increments  $\Delta t$ , with hydrogen assisted degradation ( $k_{g,L} = 0.16$  wppm<sup>-1</sup>), showing the coupled effects. The curves without hydrogen assisted degradation are illustrated in gray. Similar trends are observed as the identified single effect trends.

Making the void nucleation process dependent on hydrogen shows similar effects (Fig. 9): a significant ductility loss can be obtained when the HESIV mechanism is assumed. Nagumo [7] reported an increase in  $f_N$  that is approximately equivalent to  $k_{n,L} = 0.75$  wppm<sup>-1</sup> for the parameters employed in this study. This particular hydrogen assisted degradation factor results in a ductility loss of over 10% when simulating a hydrogen pre-charged notched tensile test.

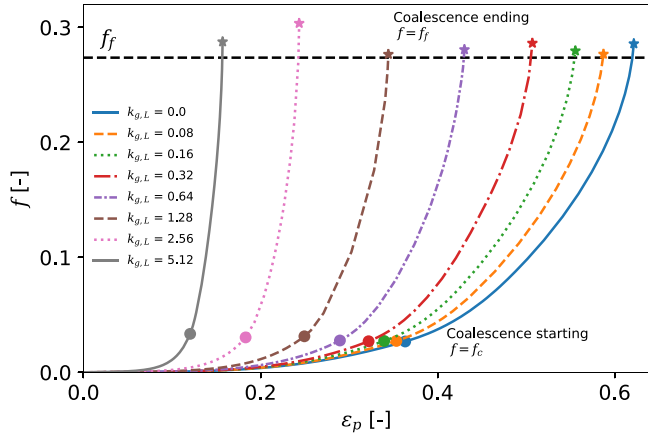
By decreasing the softening parameter  $\xi$ , the flow stress in Thomason's criterion is reduced, and accelerated coalescence occurs. Fig. 10 reports the load–elongation curve obtained with various softening parameters  $\xi$ , and a constant minimum reduction of the flow stress  $\zeta = 0.5$ . At the macroscopic level, accelerated coalescence also results in reduced elongation at failure in the simulation results of tensile loaded notched specimens. However, the ductility loss that can be obtained using this approach appears limited compared to realistic observations of HE. As such, it seems impossible to model significant manifestations of HE in a continuum way, by only changing the coalescence failure criterion. Accelerated void growth would have to be activated additionally.

### 5.2. Hydrogen diffusion

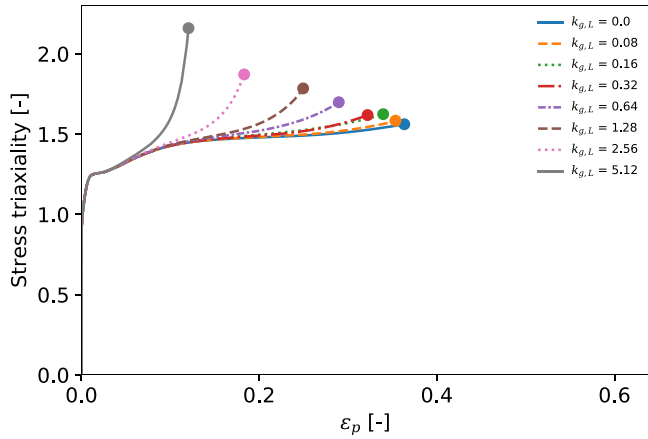
Since hydrogen assisted degradation is directly dependent on the local hydrogen concentration, the diffusion of hydrogen (Eq. (5)) is



(a)



(b)



(c)

**Fig. 8.** The effect of void growth acceleration (HELP) by varying the degradation factor  $k_{g,L}$  (wppm $^{-1}$ ) on (a) the global level in terms of load–elongation curve, (b) the local level in terms of local void volume fraction  $f$  and (c) stress triaxiality versus local plastic strain  $\epsilon_p$  of the center element. The model employed represents a tensile test on a notched hydrogen pre-charged specimen.

crucial to the observed macromechanical ductility loss. By varying the diffusion coefficient  $D_L$ , the coupling between hydrogen concentration and mechanical behavior becomes apparent.

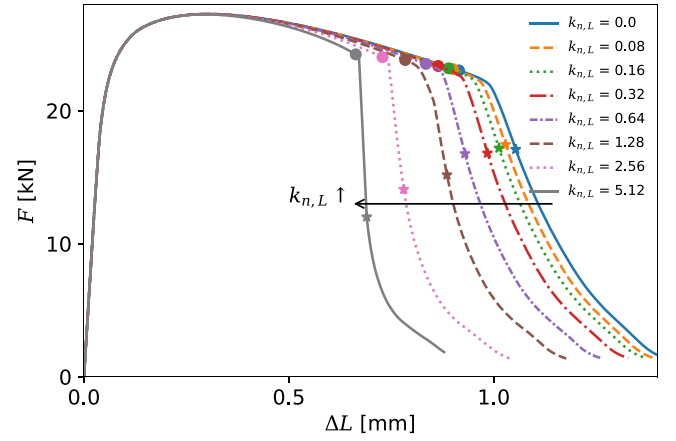


**Fig. 9.** The effect of void nucleation acceleration (HESIV) by varying the degradation factor  $k_{n,L}$  (wppm $^{-1}$ ) on the load–elongation curve.

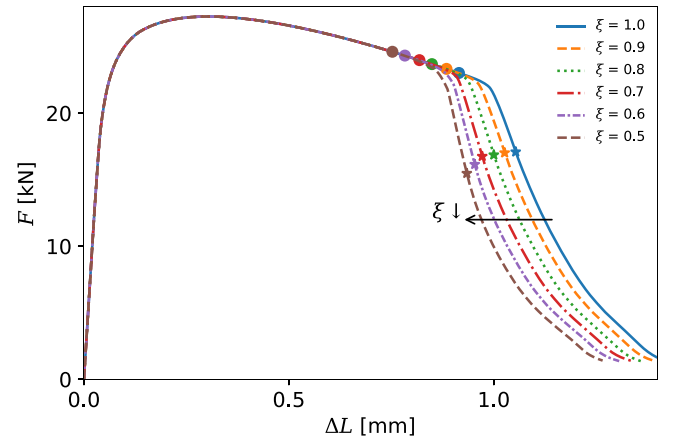


**Fig. 10.** The effect of void coalescence acceleration (HELP) by varying the degradation factor  $\xi$  on the load–elongation curve.

Hydrogen assisted degradation is employed by accelerating the void growth ( $k_{g,L} = 0.64$  wppm $^{-1}$ ), while varying the diffusion coefficient ( $D_L = 1.5 \times 10^{-5}, 1.5 \times 10^{-4}, 1.5 \times 10^{-3}, 1.5 \times 10^{-2}$  mm $^2$ /s). The other employed model parameters are equal to the parameters used in Section 5.1. Fig. 11 provides the force versus elongation curves. Due to the boundary conditions applied, hydrogen effuses out of the specimen. Hence, a larger diffusivity results in less hydrogen contributing to the accelerated damage. A large diffusion coefficient of  $1.5 \times 10^{-2}$  mm $^2$ /s results in nearly the same behavior as an uncharged specimen. Note that the macromechanical effect of an increased diffusion coefficient is equivalent to that of a lower rate of elongation.

## 6. Conclusion

This paper presents a numerical framework for hydrogen embrittlement simulations at a continuum level, combining diffusion of hydrogen with the accelerated mechanical degradation due to hydrogen in a fully coupled way. The underlying physical mechanisms in the proposed model are the plasticity dominated HE mechanisms HELP and HESIV. Damage evolution is considered through the complete Gurson model for ductile damage. The framework is implemented in the finite element software Abaqus by combining three user subroutines to allow for the prediction of the time-dependent mechanical response of the complex multi-physical problem HE.

Tensile tests on notched round bars in the presence of hydrogen were investigated numerically and the effect of the discretization

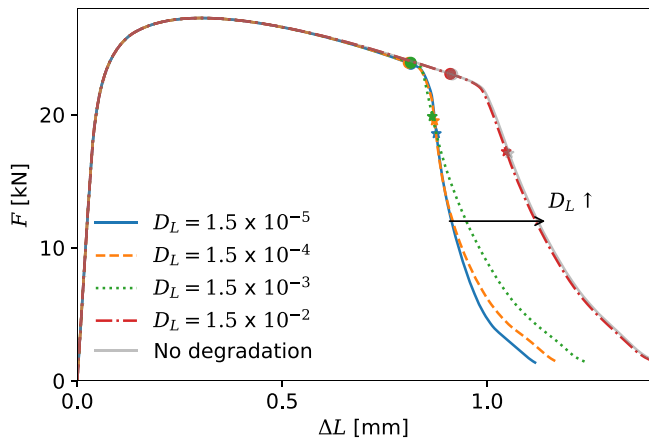


Fig. 11. The effect of lattice diffusion coefficient  $D_L$  ( $\text{mm}^2/\text{s}$ ) on the load–elongation curve of a tensile test on a notched hydrogen pre-charged specimen. Larger diffusivity results in delayed failure, since hydrogen is effusing faster out of the specimen.

parameters on the simulation results and their convergence was evaluated. The element size dependency is inherent to local damage models and should be dealt with by choosing a fixed element size. The effect of time increment is observed to be converging for smaller increments. It is proven that the degrading effect of hydrogen in terms of macromechanical ductility loss can be predicted with the proposed model. Accelerating the coalescence process, results in only limited ductility loss, suggesting that this approach individually may not suffice for modeling HELP. On the other hand, realistic ductility losses of HE tests could be obtained by accelerating either void growth or nucleation.

The calibration of the model parameters for high strength steel using dedicated experiments, and the evaluation of the effect of hydrogen on its tearing resistance by simulation of fracture toughness tests is the focus of future work.

The developed framework only considers coalescence by internal necking. A coalescence criterion describing internal shearing may be implemented for modeling more accurately the effects of HE in the low-triaxiality regime.

#### CRedit authorship contribution statement

**Robin Depraetere:** Conceptualization, Methodology, Software, Writing – original draft. **Wim De Waele:** Conceptualization, Supervision, Writing – review & editing. **Stijn Hertelé:** Conceptualization, Supervision, Writing – review & editing, Funding acquisition.

#### Declaration of competing interest

The authors declare that they have no known competing financial interests or personal relationships that could have appeared to influence the work reported in this paper.

#### Data availability

The data that support the findings of this study are available from the corresponding author upon reasonable request.

#### Acknowledgments

The authors acknowledge the support from Research Foundation - Flanders (FWO), Belgium via grant G056519N. The authors also acknowledge the assistance of Kim Verbeken and Tom Depover.

#### References

- [1] European Commission, Clean energy, 2020, URL <https://ec.europa.eu/info/strategy/priorities-2019-2024/european-green-deal/clean-energy>.
- [2] R.P. Gangloff, B.P. Somerday, Gaseous Hydrogen Embrittlement of Materials in Energy Technologies: the Problem, Its Characterisation and Effects on Particular Alloy Classes, Woodhead Publishing Limited, 2012, <http://dx.doi.org/10.2307/2524560>.
- [3] W. Johnson, On some remarkable changes produced in iron and steel by the action of hydrogen and acids, in: Proceedings of the Royal Society of London, 1875, pp. 168–179.
- [4] S.P. Lynch, Hydrogen embrittlement (HE) phenomena and mechanisms, Stress Corros. Crack.: Theory Pract. (i) (2011) 90–130, <http://dx.doi.org/10.1533/9780857093769.1.90>.
- [5] A.R. Troiano, The role of hydrogen and other interstitials in the mechanical behavior of metals, Trans. ASM 52 (1960) 54–80, URL <http://ci.nii.ac.jp/naid/10024044710/en/>.
- [6] C.D. Beachem, A new model for hydrogen-assisted cracking (hydrogen "embrittlement"), Metall. Trans. 3 (2) (1972) 441–455, <http://dx.doi.org/10.1007/BF02642048>.
- [7] M. Nagumo, Hydrogen related failure of steels - A new aspect, Mater. Sci. Technol. 20 (8) (2004) 940–950, <http://dx.doi.org/10.1179/026708304225019687>.
- [8] D. Di Stefano, R. Nazarov, T. Hickel, J. Neugebauer, M. Mrovec, C. Elsässer, First-principles investigation of hydrogen interaction with TiC precipitates in  $\alpha$ -Fe, Phys. Rev. B 93 (18) (2016) 1–14, <http://dx.doi.org/10.1103/PhysRevB.93.184108>.
- [9] J. Song, W.A. Curtin, Mechanisms of hydrogen-enhanced localized plasticity: An atomistic study using  $\alpha$ -Fe as a model system, Acta Mater. 68 (2014) 61–69, <http://dx.doi.org/10.1016/j.actamat.2014.01.008>.
- [10] A. Tehranchi, W.A. Curtin, The role of atomistic simulations in probing hydrogen effects on plasticity and embrittlement in metals, Eng. Fract. Mech. 216 (May) (2019) 106502, <http://dx.doi.org/10.1016/j.engfractmech.2019.106502>.
- [11] S.S. Shishvan, G. Csányi, V.S. Deshpande, Hydrogen induced fast-fracture, J. Mech. Phys. Solids 134 (2020) 103740, <http://dx.doi.org/10.1016/j.jmps.2019.103740>.
- [12] O. Barrera, D. Bombac, Y. Chen, T.D. Daff, E. Galindo-Nava, P. Gong, D. Haley, R. Horton, I. Katzarov, J.R. Kermode, C. Liverani, M. Stopher, F. Sweeney, Understanding and mitigating hydrogen embrittlement of steels: a review of experimental, modelling and design progress from atomistic to continuum, J. Mater. Sci. 53 (9) (2018) 6251–6290, <http://dx.doi.org/10.1007/s10853-017-1978-5>.
- [13] E. Tarleton, Incorporating hydrogen in mesoscale models, Comput. Mater. Sci. 163 (April) (2019) 282–289, <http://dx.doi.org/10.1016/j.commatsci.2019.03.020>.
- [14] E. Ogosi, A. Siddiq, U.B. Asim, M.E. Kartal, Hydrogen effect on plastic deformation and fracture in austenitic stainless steel, in: CORROSION 2020, NACE International, physical event cancelled, 2020, p. 19.
- [15] V. Olden, C. Thaulow, R. Johnsen, E. Østby, T. Berstad, Application of hydrogen influenced cohesive laws in the prediction of hydrogen induced stress cracking in 25%Cr duplex stainless steel, Eng. Fract. Mech. 75 (8) (2008) 2333–2351, <http://dx.doi.org/10.1016/j.engfractmech.2007.09.003>.
- [16] H. Yu, J.S. Olsen, A. Alvaro, V. Olden, J. He, Z. Zhang, A uniform hydrogen degradation law for high strength steels, Eng. Fract. Mech. 157 (2016) 56–71, <http://dx.doi.org/10.1016/j.engfractmech.2016.02.001>.
- [17] S. Huang, Y. Zhang, C. Yang, H. Hu, Fracture strain model for hydrogen embrittlement based on hydrogen enhanced localized plasticity mechanism, Int. J. Hydrogen Energy 45 (46) (2020) 25541–25554, <http://dx.doi.org/10.1016/j.ijhydene.2020.06.271>.
- [18] J. Lufano, P. Sofronis, H.K. Birnbaum, Elastoplastically accommodated hydride formation and embrittlement, J. Mech. Phys. Solids 46 (9) (1998) 1497–1520, [http://dx.doi.org/10.1016/S0022-5096\(98\)00054-4](http://dx.doi.org/10.1016/S0022-5096(98)00054-4).
- [19] A. Díaz, J.M. Alegre, I.I. Cuesta, Coupled hydrogen diffusion simulation using a heat transfer analogy, Int. J. Mech. Sci. 115–116 (2016) 360–369, <http://dx.doi.org/10.1016/j.ijmecsci.2016.07.020>.
- [20] V. Olden, C. Thaulow, R. Johnsen, E. Østby, T. Berstad, Influence of hydrogen from cathodic protection on the fracture susceptibility of 25%Cr duplex stainless steel - constant load sent testing and FE-modelling using hydrogen influenced cohesive zone elements, Eng. Fract. Mech. 76 (7) (2009) 827–844, <http://dx.doi.org/10.1016/j.engfractmech.2008.11.011>.
- [21] V. Olden, A. Alvaro, O.M. Akselsen, Hydrogen diffusion and hydrogen influenced critical stress intensity in an API X70 pipeline steel welded joint-experiments and FE simulations, Int. J. Hydrogen Energy 37 (15) (2012) 11474–11486, <http://dx.doi.org/10.1016/j.ijhydene.2012.05.005>.
- [22] A. Alvaro, V. Olden, O.M. Akselsen, 3D cohesive modelling of hydrogen embrittlement in the heat affected zone of an X70 pipeline steel, Int. J. Hydrogen Energy 38 (18) (2013) 7539–7549, <http://dx.doi.org/10.1016/j.ijhydene.2013.02.146>.
- [23] A. Alvaro, V. Olden, O.M. Akselsen, 3D cohesive modelling of hydrogen embrittlement in the heat affected zone of an X70 pipeline steel - Part II, Int. J. Hydrogen Energy 39 (7) (2014) 3528–3541, <http://dx.doi.org/10.1016/j.ijhydene.2013.12.097>.



- [24] G. Gobbi, C. Colombo, S. Miccoli, L. Vergani, A weakly coupled implementation of hydrogen embrittlement in fe analysis, *Finite Elem. Anal. Des.* 141 (November 2017) (2018) 17–25, <http://dx.doi.org/10.1016/j.finel.2017.11.010>.
- [25] W. Brocks, R. Falkenberg, I. Scheider, Coupling aspects in the simulation of hydrogen-induced stresscorrosion cracking, in: *Procedia IUTAM*, Vol. 3, 2012, pp. 11–24, <http://dx.doi.org/10.1016/j.piutam.2012.03.002>.
- [26] O. Barrera, E. Tarleton, H.W. Tang, A.C. Cocks, Modelling the coupling between hydrogen diffusion and the mechanical behaviour of metals, *Comput. Mater. Sci.* 122 (2016) 219–228, <http://dx.doi.org/10.1016/j.commatsci.2016.05.030>.
- [27] G. Gobbi, C. Colombo, S. Miccoli, L. Vergani, A fully coupled implementation of hydrogen embrittlement in fe analysis, *Adv. Eng. Softw.* 135 (July) (2019) 102673, <http://dx.doi.org/10.1016/j.advengsoft.2019.04.004>.
- [28] H. Yu, J.S. Olsen, A. Alvaro, L. Qiao, J. He, Z. Zhang, Hydrogen informed gursen model for hydrogen embrittlement simulation, *Eng. Fract. Mech.* 217 (February) (2019) 106542, <http://dx.doi.org/10.1016/j.engfracmech.2019.106542>.
- [29] D.C. Ahn, P. Sofronis, R. Dodds, Modeling of hydrogen-assisted ductile crack propagation in metals and alloys, *Int. J. Fract.* 145 (2) (2007) 135–157, <http://dx.doi.org/10.1007/s10704-007-9112-3>.
- [30] L. Jemblie, V. Olden, O.M. Akselsen, A coupled diffusion and cohesive zone modelling approach for numerically assessing hydrogen embrittlement of steel structures, *Int. J. Hydrogen Energy* 42 (16) (2017) 11980–11995, <http://dx.doi.org/10.1016/j.ijhydene.2017.02.211>.
- [31] S. del Busto, C. Betegón, E. Martínez-Pañeda, A cohesive zone framework for environmentally assisted fatigue, *Eng. Fract. Mech.* (2017) <http://dx.doi.org/10.1016/j.engfracmech.2017.05.021>, URL [arXiv:1711.09965](https://arxiv.org/abs/1711.09965).
- [32] V.T. Vanapalli, B.K. Dutta, J. Chattopadhyay, N.M. Jose, Stress triaxiality based transferability of cohesive zone parameters, *Eng. Fract. Mech.* 224 (2020) <http://dx.doi.org/10.1016/j.engfracmech.2019.106789>.
- [33] E. Martínez-Pañeda, A. Golahmar, C.F. Niordson, A phase field formulation for hydrogen assisted cracking, *Comput. Methods Appl. Mech. Engrg.* 342 (2018) 742–761, <http://dx.doi.org/10.1016/j.cma.2018.07.021>, URL [arXiv:1808.03264](https://arxiv.org/abs/1808.03264).
- [34] E. Martínez-Pañeda, Z.D. Harris, S. Fuentes-Alonso, J.R. Scully, J.T. Burns, On the suitability of slow strain rate tensile testing for assessing hydrogen embrittlement susceptibility, *Corros. Sci.* 163 (2020) <http://dx.doi.org/10.1016/j.corsci.2019.108291>, URL [arXiv:1910.07983](https://arxiv.org/abs/1910.07983).
- [35] H. Yu, J.S. Olsen, J. He, Z. Zhang, Hydrogen-microvoid interactions at continuum scale, *Int. J. Hydrogen Energy* 43 (21) (2018) 10104–10128, <http://dx.doi.org/10.1016/j.ijhydene.2018.04.064>.
- [36] R. Garber, I.M. Bernstein, A.W. Thompson, Effect of hydrogen on ductile fracture of spheroidized steel, *Scr. Metall.* 10 (4) (1976) 341–345.
- [37] R. Garber, I.M. Bernstein, A.W. Thompson, Hydrogen assisted ductile fracture of spheroidized carbon steels, *Metall. Trans. A* 12 (2) (1981) 225–234, <http://dx.doi.org/10.1007/BF02655195>.
- [38] H. Cialone, R.J. Asaro, The role of hydrogen in the ductile fracture of plain carbon steels, *Metall. Trans. A* 10 (3) (1979) 367–375, <http://dx.doi.org/10.1007/BF02658347>.
- [39] T. Matsuo, N. Homma, S. Matsuoka, Y. Murakami, Effect of hydrogen and prestrain on tensile properties of carbon steel SGP (0.078 C-0.012 Si-0.35 Mn, mass%) for 0.1 MPa hydrogen pipelines, *Nihon Kikai Gakkai Ronbunshu, A Hen/Trans. Japan Soc. Mech. Eng. A* 74 (744) (2008) 1164–1173, <http://dx.doi.org/10.1299/kikaia.74.1164>.
- [40] Z.L. Zhang, C. Thaulow, J. Ødegård, Complete gursen model approach for ductile fracture, *Eng. Fract. Mech.* 67 (2) (2000) 155–168, [http://dx.doi.org/10.1016/S0013-7944\(00\)00055-2](http://dx.doi.org/10.1016/S0013-7944(00)00055-2).
- [41] P. Sofronis, R.M. McMeeking, Numerical analysis of hydrogen transport near a blunting crack tip, *J. Mech. Phys. Solids* 37 (3) (1989) 317–350, [http://dx.doi.org/10.1016/0022-5096\(89\)90002-1](http://dx.doi.org/10.1016/0022-5096(89)90002-1).
- [42] A.J. Kunnick, H.H. Johnson, Deep trapping states for hydrogen in deformed iron, *Acta Metall.* 28 (1) (1980) 33–39, [http://dx.doi.org/10.1016/0001-6160\(80\)90038-3](http://dx.doi.org/10.1016/0001-6160(80)90038-3), URL <http://www.sciencedirect.com/science/article/pii/0001616080900383>.
- [43] R.A. Oriani, The diffusion and trapping of hydrogen in steel, *Acta Metall.* 18 (1) (1970) 147–157, [http://dx.doi.org/10.1016/0001-6160\(70\)90078-7](http://dx.doi.org/10.1016/0001-6160(70)90078-7).
- [44] A.H. Krom, R.W. Koers, A. Bakker, Hydrogen transport near a blunting crack tip, *J. Mech. Phys. Solids* 47 (4) (1999) 971–992, [http://dx.doi.org/10.1016/S0022-5096\(98\)00064-7](http://dx.doi.org/10.1016/S0022-5096(98)00064-7).
- [45] M. Dadfarnia, P. Sofronis, T. Neeraj, Hydrogen interaction with multiple traps: Can it be used to mitigate embrittlement? *Int. J. Hydrogen Energy* 36 (16) (2011) 10141–10148, <http://dx.doi.org/10.1016/j.ijhydene.2011.05.027>.
- [46] A.L. Gursen, Continuum theory of ductile rupture by void nucleation and growth: Part 1 - yield criteria and flow rules for porous ductile media, *J. Eng. Mater. Technol. Trans. ASME* 99 (1) (1977) 2–15, <http://dx.doi.org/10.1115/1.3443401>.
- [47] B. Younise, M. Rakin, N. Gubeljak, B. Medjo, A. Sedmak, Effect of material heterogeneity and constraint conditions on ductile fracture resistance of welded joint zones - micromechanical assessment, *Eng. Fail. Anal.* 82 (August) (2017) 435–445, <http://dx.doi.org/10.1016/j.engfailanal.2017.08.006>.
- [48] A. Sedmak, M. Rakin, B. Medjo, B. Younise, Micromechanical modelling of ductile fracture - local approach, *Metall. Mater. Eng.* 25 (4) (2019) 265–286, <http://dx.doi.org/10.30544/459>.
- [49] J. Xu, W. Song, W. Cheng, L. Chu, H. Gao, P. Li, F. Berto, Modelling of fracture toughness of X80 pipeline steels in DTB transition region involving the effect of temperature and crack growth, *Metals* 10 (1) (2020) <http://dx.doi.org/10.3390/met10010028>.
- [50] Y. Zhang, J. Shuai, Z. Lv, K. Xu, Investigation of the effects of material parameters on the relationship between crack tip constraint and CTOD fracture toughness, *Theor. Appl. Fract. Mech.* 108 (2020) <http://dx.doi.org/10.1016/j.tafmec.2020.102615>.
- [51] A. Pineau, A.A. Benzerga, T. Pardoen, Failure of metals I: Brittle and ductile fracture, *Acta Mater.* 107 (2016) 424–483, <http://dx.doi.org/10.1016/j.actamat.2015.12.034>.
- [52] V. Tvergaard, A. Needleman, Analysis of the cup-cone fracture in a round tensile bar, *Acta Metall.* 32 (1) (1984) 157–169, [http://dx.doi.org/10.1016/0001-6160\(84\)90213-X](http://dx.doi.org/10.1016/0001-6160(84)90213-X), URL <http://www.sciencedirect.com/science/article/pii/000161608490213X>.
- [53] C.C. Chu, A. Needleman, Void nucleation effects in biaxially stretched sheets, *Journal of Engineering Materials and Technology, Transactions of the ASME* 102 (3) (1980) 249–256, <http://dx.doi.org/10.1115/1.3224807>.
- [54] V.D. Nguyen, T. Pardoen, L. Noels, A nonlocal approach of ductile failure incorporating void growth, internal necking, and shear dominated coalescence mechanisms, *J. Mech. Phys. Solids* 137 (2020) 103891, <http://dx.doi.org/10.1016/j.jmps.2020.103891>.
- [55] R. Kiran, K. Khandelwal, Gursen model parameters for ductile fracture simulation in ASTM A992 steels, *Fatigue Fract. Eng. Mater. Struct.* 37 (2) (2014) 171–183, <http://dx.doi.org/10.1111/ffe.12097>.
- [56] K. Danas, P. Ponte Castañeda, Influence of the lode parameter and the stress triaxiality on the failure of elasto-plastic porous materials, *Int. J. Solids Struct.* 49 (11–12) (2012) 1325–1342, <http://dx.doi.org/10.1016/j.ijsolstr.2012.02.006>.
- [57] P.F. Thomason, Three-dimensional models for the plastic limit-loads at incipient failure of the intervoid matrix in ductile porous solids, *Acta Metall.* 33 (6) (1985) 1079–1085, [http://dx.doi.org/10.1016/0001-6160\(85\)90201-9](http://dx.doi.org/10.1016/0001-6160(85)90201-9).
- [58] F. Rahimidehghan, G. Majzoobi, F. Alinejad, J.F. Sola, Determination of the constants of GTN damage model using experiment, polynomial regression and kriging methods, *Appl. Sci. (Switzerland)* 7 (11) (2017) 1179, <http://dx.doi.org/10.3390/app7111179>.
- [59] D.C. Ahn, P. Sofronis, R.H. Dodds, On hydrogen-induced plastic flow localization during void growth and coalescence, *Int. J. Hydrogen Energy* 32 (16) (2007) 3734–3742, <http://dx.doi.org/10.1016/j.ijhydene.2006.08.047>.
- [60] T. Luo, C. Huang, X. Gao, An investigation of the effect of hydrogen on ductile fracture using a unit cell model, *Int. J. Hydrogen Energy* 44 (16) (2019) 8627–8640, <http://dx.doi.org/10.1016/j.ijhydene.2019.02.069>.
- [61] A. Díaz, J.M. Alegre, I.I. Cuesta, Z. Zhang, Numerical study of hydrogen influence on void growth at low triaxialities considering transient effects, *Int. J. Mech. Sci.* (2019) <http://dx.doi.org/10.1016/j.ijmecsci.2019.105176>.
- [62] Dassault Systemes, Abaqus documentation, 2019, URL <https://help.3ds.com/HelpProductsDS.aspx>.
- [63] C.-S. Oh, Y.-J. Kim, K.-B. Yoon, Coupled analysis of hydrogen transport using ABAQUS, *J. Solid Mech. Mater. Eng.* 4 (7) (2010) 908–917, <http://dx.doi.org/10.1299/jmmp.4.908>.
- [64] S.G. Larsson, A.J. Carlsson, Influence of non-singular stress terms and specimen geometry on small-scale yielding at crack tips in elastic-plastic materials, *J. Mech. Phys. Solids* 21 (4) (1973) 263–277, [http://dx.doi.org/10.1016/0022-5096\(73\)90024-0](http://dx.doi.org/10.1016/0022-5096(73)90024-0).
- [65] M. Verstraete, W. De Waele, S. Hertele, Development and validation of a high constraint modified boundary layer finite element model, *Sustain. Constr. Des.* 2 (2) (2011) 228–236.
- [66] J. Besson, Continuum Models of Ductile Fracture: A Review, Vol. 19, SAGE Publications, 2010, pp. 3–52, <http://dx.doi.org/10.1177/1056789509103482>.
- [67] A. Pineau, T. Pardoen, 2.06 - failure of metals, in: *Comprehensive Structural Integrity*, Vol. 2, Elsevier Ltd, 2007, pp. 684–797, <http://dx.doi.org/10.1016/B0-08-043749-4/02109-1>.
- [68] P.W. Bridgman, Studies in Large Plastic Flow and Fracture with Special Emphasis on the Effects of Hydrostatic Pressure, McGraw-Hill, New York (N.Y.), 1952, URL <http://lib.ugent.be/catalog/rug01:000320116>.
- [69] American Petroleum Institute, API Specification 5L - Line Pipe, (46) 2018.
- [70] C. Qian, Investigation of Ductile Crack Growth and Normalization Method for SE(T) Specimen Using Finite Element Analyses (Ph.D. thesis), (December) Western University, 2017.
- [71] M. Seidenfuss, T. Linse, Micromechanical-based models for describing damage of ferritic steels, in: *Recent Trends in Fracture and Damage Mechanics*, Springer, 2016, pp. 353–416, [http://dx.doi.org/10.1007/978-3-319-21467-2\\_16](http://dx.doi.org/10.1007/978-3-319-21467-2_16).
- [72] Z.L. Zhang, On the accuracies of numerical integration algorithms for gursen-based pressure-dependent elastoplastic constitutive models, in: *Computer Methods in Applied Mechanics and Engineering*, Vol. 121, (1–4) 1995, pp. 15–28, [http://dx.doi.org/10.1016/0045-7825\(94\)00706-S](http://dx.doi.org/10.1016/0045-7825(94)00706-S).
- [73] A. Seupel, G. Hütter, M. Kuna, On the identification and uniqueness of constitutive parameters for a non-local GTN-model, *Eng. Fract. Mech.* 229 (2020) 106817, <http://dx.doi.org/10.1016/j.engfracmech.2019.106817>, URL <https://linkinghub.elsevier.com/retrieve/pii/S0013794419306769>.



- [74] S.P. Trasatti, E. Sivieri, F. Mazza, Susceptibility of a X80 steel to hydrogen embrittlement, *Mater. Corros.* 56 (2) (2005) 111–117, <http://dx.doi.org/10.1002/maco.200403821>.
- [75] I. Moro, L. Briottet, P. Lemoine, E. Andrieu, C. Blanc, G. Odemer, Hydrogen embrittlement susceptibility of a high strength steel X80, *Mater. Sci. Eng. A* 527 (27–28) (2010) 7252–7260, <http://dx.doi.org/10.1016/j.msea.2010.07.027>.
- [76] M. Hassan, R.A. Overfelt, Microstructurally mediated changes in fracture characteristics for electrochemically hydrogenated 4340 steel, *Mater. Perform. Charact.* 4 (2) (2015) 68–83, <http://dx.doi.org/10.1520/MPC20140026>.